Preprint Cambridge Centre for Computational Chemical Engineering ISSN 1473 – 4273

Degree of crosslinking in combustion carbons

Laura Pascazio[1], Jacob W. Martin[1], Maria L. Botero[2], Mariano Sirignano[3], Andrea D'Anna[3] and Markus Kraft[1,4,5]

released: 18 June 2018

[1] Department of Chemical Engineering
and Biotechnology
University of Cambridge
West Site
Philippa Fawcett Drive
Cambridge, CB3 0AS
United Kingdom
E-mail: mk306@cam.ac.uk

[2] Department of Mechanical Engineering
National University of Singapore
9 Engineering Drive
Singapore, 117576

[3] Dipartimento di Ingegneria Chimica,
dei Materiali e della Produzione Industriale
Università degli Studi di Napoli Federico II
Piazzale V. Tecchio 80
Napoli, 80125
Italy

[4] School of Chemical and
Biomedical Engineering
Nanyang Technological University
62 Nanyang Drive
Singapore, 637459

[5] Cambridge Centre for Advanced Research
and Education in Singapore (CARES)
CREATE Tower
1 Create Way
Singapore, 138602

Preprint No. 205

Keywords: molecular dynamics, reactive force field, hardness, crosslinking, carbonisation

Edited by
Computational Modelling Group
Department of Chemical Engineering and Biotechnology
University of Cambridge
West Site, Philippa Fawcett Drive
Cambridge, CB3 0AS
United Kingdom

Fax: + 44 (0)1223 334796
E-Mail: c4e@cam.ac.uk
World Wide Web: http://como.cheng.cam.ac.uk/

Abstract

In this paper, we estimate the degree of crosslinking within soot particles and carbon blacks making use of reactive force field molecular dynamics simulations of the mechanical properties of crosslinked polycyclic aromatic hydrocarbons (PAHs). Representative systems of PAHs with a density similar to nascent soot and with varying degrees of crosslinking were built. The yield stress and hardness of each sample were calculated and the results compared with nanoindentation experiments of soot particles. The results indicate that the ethylene and diesel soot degree of crosslinking is between 2.25–2.75 and 2.85–3.15 respectively. Further evidence of a three-dimensional network of crosslinks between PAHs in soot structure has been found from electron microscopy experiments. Electron microscopy image simulations demonstrate that kinked fringes observed in the electron micrographs can be interpreted as crosslinked PAHs. High resolution transmission electron micrographs of soot primary particles with fringe statistics were also analysed as a function of the radius for the first time, giving quantitative information about the soot core-shell structure and soot maturation. All the results indicate that a crosslinking process with subsequent carbonisation is taking place during soot formation, giving rise to a structure in which the majority of aromatics are aliphatically-linked with some ring condensations.

Highlights

- Mechanical properties of crosslinked polycyclic aromatic hydrocarbons (PAHs) are investigated, making use of reactive molecular dynamics simulations.
- The degree of crosslinking of ethylene and diesel soot is between 2.25–2.75 and 2.85–3.15 respectively to have a comparable value of the hardness found experimentally.
- Electron microscopy image simulations demonstrate that kinked fringes in high resolution transmission electron microscopy (HRTEM) images of soot primary particles can be interpreted as crosslinked PAHs.
- HRTEM experiments of soot primary particles with radial fringe statistics give further evidence of the presence of a 3D network of crosslinked PAHs in soot.

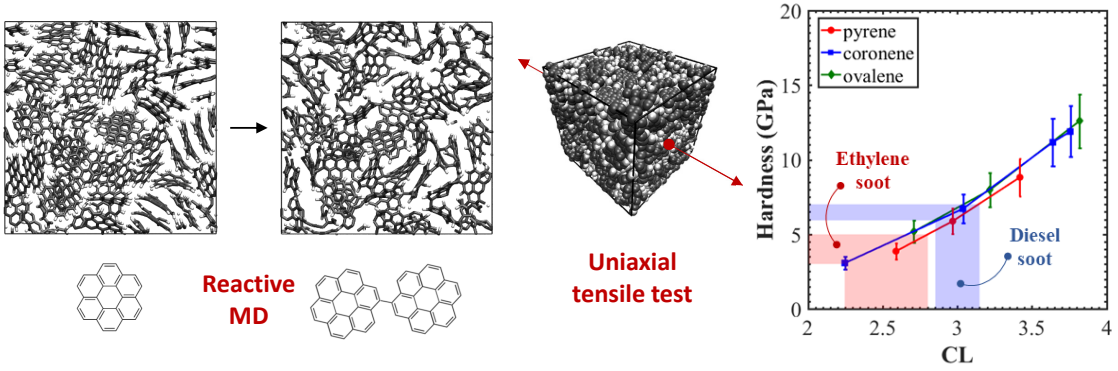

Contents

1 Introduction

Carbonaceous particles produced during combustion present a pressing problem to human health and the climate [7, 35, 41], but can also produce many novel carbon materials used as pigments, reinforcing rubbers and battery anodes [67]. Both goals - destroying the soot and controlling the synthesis of carbon blacks - require an understanding of the chemistry and morphology of the carbon particles.

The complexity of the soot nucleation process makes its study challenging experimentally and computationally. Polycyclic aromatic hydrocarbons (PAHs) are widely accepted as precursors of soot particles [16, 19, 25, 67]. Three primary nucleation pathways have been postulated for soot nucleation [67]: the formation of fullerene-like structures as the nuclei for soot particles [30], the physical nucleation of planar PAHs into stacked clusters [26, 29, 51] and the chemical nucleation of PAHs into crosslinked three-dimensional structures [14, 50, 65, 66]. All the above mechanisms are believed to take part in the soot nucleation process, but their relative importance or feasibility at different conditions and temperatures is still unclear.

The physical nucleation pathway of soot, which is the only mechanism rapid enough to explain the inception process [67], has been explored in previous studies utilising different atomic simulation methods, such as density functional theory [71], molecular dynamics (MD) [13, 37, 51, 61, 62], Monte Carlo [48] and well-tempered metadynamics simulations [21, 22]. Many different kinds of PAHs that differ in size and structure have been investigated as particle precursors over the years. These include pericondensed aromatic hydrocarbons [13, 51, 61, 62], aromatic compounds with heteroatoms [22] and pentagonal rings [68, 69], as well as the presence of aliphatic side chains [13, 21]. All these studies have shown that the physical interactions between medium-sized PAHs are not strong enough to stabilise the clusters at high temperatures, and only aromatic molecules as big as circumcoronene were found to be able to dimerise at temperatures where soot forms ($\approx$1500 K). Understanding the degree of crosslinking in early soot particles is therefore important for determining which mechanisms and precursors are involved in their inception.

From an experimental perspective, the primary particles (10–50 nm) making up the aggregates are known to consist of aromatic layers with some degree of ordering often referred to as basic structural units [2]. Early models of carbon blacks and soot proposed a homogeneous distribution of these structural units throughout the primary particles [56]. However, the advent of electron microscopy revealed an internal structure to these particles, indicating a core-shell structure with less structured nuclei inside of carbon blacks [20, 27, 28] and potentially multiple nuclei [31]. Figure 1 illustrates this for the internal structure of soot primary particles along the wings of a co-flow diffusion flame. The development of a core-shell structure has been correlated with the maturity of the particle, with the C/H ratio and band gap decreasing with height above the burner [15, 17, 33]. High resolution transmission electron microscopy (HRTEM) images also showed fringe lengths increasing and interplane distances decreasing with soot maturity and the flame temperature [2–4, 33]. These observations have been interpreted as an indication that carbonisation processes are occurring from the outside in, which could impact the gas phase chemistry by evolving hydrogen as well as the reactivity of these particles [27, 52].

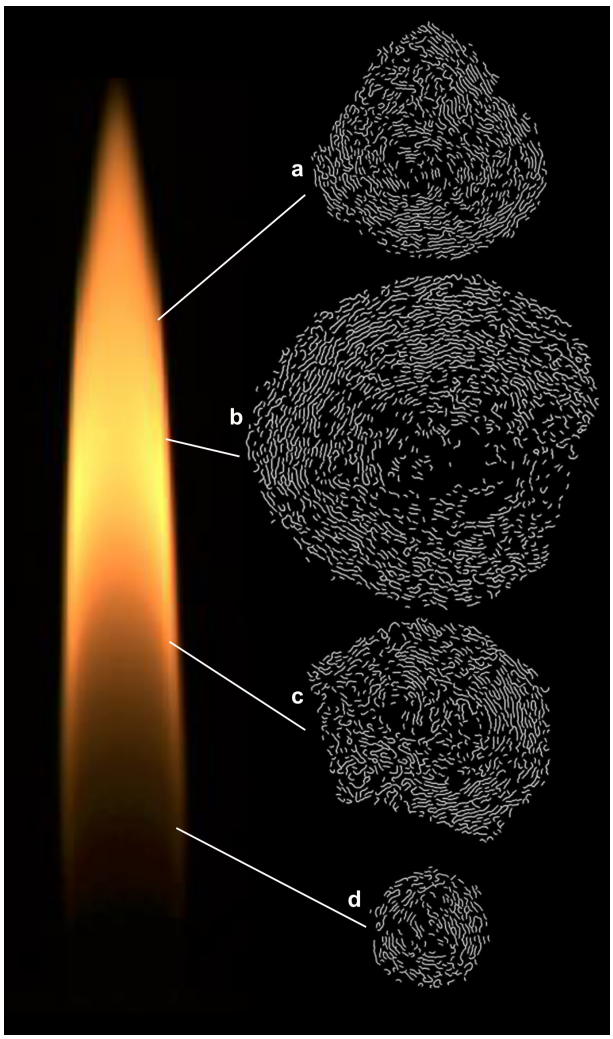

Figure 1: *Skeletonised fringes determined from HRTEM images of primary particles from soot produced in an ethylene co-flow diffusion flame showing a less ordered core and shell structure developing for heights above the burner a-d) 43, 31, 20 and 10 mm.*

Carbonisation of PAHs is known to occur through a radical mechanism initially forming an aliphatic crosslink followed by dehydrogenation and ring formation [36, 58, 63]. While there is no direct evidence of crosslinked PAHs in soot particles, nanoindentation suggests significant crosslinks when compared with non-crosslinked nanocrystalline graphite, which has yet to feature prominently in discussions of soot and carbon blacks [5, 6]. Nanoindentation measures the force as a well-defined tip is pushed into a material from which the hardness (H) can be determined – $H = P_{max}/A_r$ where P_{max} is the maximum load and A_r the indentation area. Table 1 summarises the findings from nanoindentation studies of various carbon materials. The relative hardness of the different carbon materials can provide an indicator for the degree of crosslinking. Nanocrystalline graphite is known to be an uncrosslinked structure made of mobile graphene sheets with a very low hardness (0.1–0.4 GPa). Nanoindentation studies of amorphous carbon film containing crosslinked

nanocrystalline graphite clusters indicate that hardness increases with sp^3 bond content in the structure [23]. Looking at the hardness values of mature soot and carbon blacks, values closer to a hard crosslinked carbon such as charcoal are found. These results indicate that mature soot and carbon blacks are probably carbonised and crosslinked and are not van der Waals solids. This is also supported by chromatography where soot extracted in a fuel-rich premixed ethylene flame contains an initially eluted fraction with PAHs of masses m/z 300–600, determined from laser desorption time of flight mass spectrometry and a secondary peak of polymerised products matching that of pitch made from polymerised naphthalene [1]. These results support the idea of carbonisation beginning with single aliphatic bonds forming between aromatic molecules.

Table 1: *Table of carbon-based materials hardness values from nanoindentation.*

Material	Hardness (GPa)	Ref.
Nanocrystalline graphite	0.1–0.4	[44]
HOPG	2.4	[49]
Carbon black	3–4	[5]
Ethylene soot	3–5	[5, 6]
Charcoal	3–5	[73]
Diesel soot	6–7	[5]
Polymerised C_{70}	30	[44]
Glassy carbon	30	[32]
Diamond	100	[49]

From the previous considerations, we suggest that soot particles must present crosslinks in their structure. The purpose of the present study is therefore to consider the degree of crosslinking. We constructed an idealised structure of soot described by crosslinked polycyclic aromatic hydrocarbons (PAHs). We performed reactive force field MD simulations and computed stress-strain curves of such structures. The yield stress and hardness of systems with varying degrees of crosslinking have been calculated and the degree of crosslinking within soot particles has been estimated, comparing our results with the hardness found from nanoindentation experiments of soot. The hypothesis of describing soot particles as a three-dimensional (3D) network of crosslinked PAHs has then been motivated in the second part of the paper by making use of electron microscopy. These experiments with fringe analysis of the radial profile of fringes inside primary particles have also been made to compare the results with simulated transmission electron microscopy images and to give further evidence of crosslinking and carbonisation.

2 Methodology

2.1 Molecular dynamics simulations

The MD method was employed to simulate the uniaxial tensile deformation of crosslinked PAH structures, in order to investigate the effect of the degree of crosslinking in the structure on its mechanical properties. To achieve this goal the following procedure was adopted:

1. A crosslinking procedure was developed to build PAH boxes with varying degree of crosslinking.
2. Uniaxial tensile deformation tests were carried out on the selected structure and their yield stress and hardness were evaluated.
3. The MD results were compared with experimental data.

Every part will be described in detail in the following sections. A schematic diagram of the adopted methodology is reported in Fig. 2.

The reactive force field MD simulations were carried out using the LAMMPS software [45]. Pyrene, coronene and ovalene were chosen as starting monomers as spanning the size range of fragments found in early soot particles [8]. The interactions within molecules were modelled using an updated version of the adaptive intermolecular reactive empirical bond order (AIREBO) potential [55], known as AIREBO-M [42], which has been widely used to investigate the mechanical and thermal properties of carbon-based nanomaterials. AIREBO-M uses the same functional form as the hydrocarbon second-generation REBO potential [10], with an additional Morse term to represent the Van der Waals interactions. The Morse potential replaces the Lennard-Jones potential used in the original AIREBO, which has been shown to yield unphysical results for carbon systems subjected to high pressures [42]. The Morse potentials are parameterised by high-quality quantum chemistry calculations and do not diverge as quickly as the Lennard-Jones potentials when particle density increases. This allows AIREBO-M to retain accuracy to much higher material densities than AIREBO.

2.1.1 Crosslinking procedure

The crosslinking procedure was realised as follows:

1. Homomolecular systems of the three PAH molecules considered (pyrene, coronene and ovalene) were built. Monomers were randomly located in a cubic simulation box using the PACKMOL software [39] (step 1 in Fig. 2). The number of molecules were chosen to have a starting cubic box with side length 43 Å and a density of 1.5 g/cm^3, which is a typical value for nascent soot particles [72]. The initial uncrosslinked structure was firstly minimised and then equilibrated for 200 ps in the

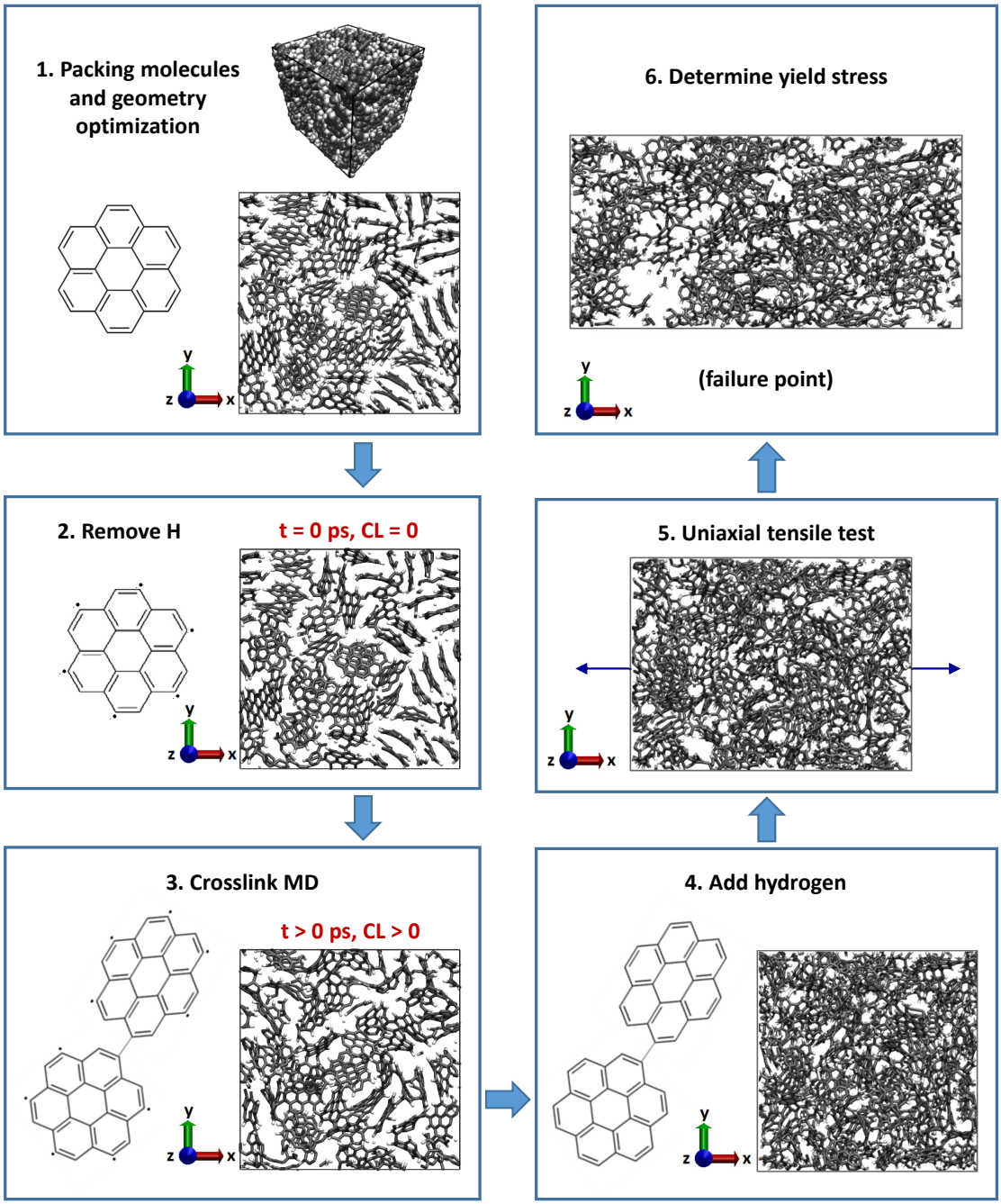

Figure 2: *The steps involved in the crosslinking simulations: 1. the aromatic molecules are packed into the simulation box; 2. hydrogen atoms are removed from every second carbon atom around the rim of the molecule; 3. a reactive force field simulation is run and halted at different times to provide varying degrees of crosslinking; 4. hydrogen atoms are then added back to the sites that have not formed crosslinks; 5. and 6. the structure is uniaxially strained until failure. The images show slices of the simulation box of 10 Å thickness for step 1, 2 and 3 and of 20 Å thickness for step 4, 5 and 6.*

isothermal and isochoric ensemble (NVT) at 300 K with a corresponding integration time step of 0.5 fs with periodic boundary conditions. The constant temperature was controlled by the Berendsen thermostat, with a time constant of 0.1 ps. Due to the periodic boundary conditions, covalent bonds can form not only between the monomers inside the simulation cell, but also between monomers across the periodic boundaries. Therefore, this step is necessary to ensure a good distribution of molecules also in the boundary region. It was verified that, avoiding this step, the crosslink density in the boundary region is lower with respect to the density in the central region, so that, during the tensile test, the structure fails near the boundaries and the tensile test results are in error.

2. The crosslinking process starts with hydrogen removal to a consequent bond creation between molecules. The reactive sites were created in the simulation boxes by directly removing hydrogen atoms from every second carbon atom around the rim of the molecule (step 2 in Fig. 2). The use of a reactive potential allows for chemical bond formation to occur between pair of reactive sites. The types of crosslinks formed were the most preliminary types of crosslinks where a single aliphatic linkage joined two pericondensed aromatic molecules [36, 63]. Single crosslinks between planar PAHs causes the two aromatic planes to be non-parallel due to the steric interactions between the neighbouring hydrogen atoms and allows for 3D crosslinking to occur.

3. Reactive force field simulations in NVT ensemble were run and halted after different simulation durations to provide varying degrees of crosslinking (step 3 in Fig. 2). The degree of crosslinking (*CL*) was defined as:

$$CL = \frac{2 \cdot \text{number of crosslinks in the system}}{\text{number of starting monomers}}. \tag{1}$$

   By definition, *CL* represents the average number of crosslinks contained in each molecule in the system. It means that, when the *CL* density is 1, each molecule contains on average a singe crosslink and mainly dimers are formed. A *CL* density of 2 is required for a polymer where on average each molecule contains two crosslinks and *CL* between 2 and 3 for a 3D network.
   A time step of 0.25 fs was adopted for the integration of the atomic equations of motion and the Berendsen thermostat was used to maintain a constant temperature of 1000 K with a time constant of 0.1 ps. These simulation parameters ensured a stable simulation as significant heat had to be removed due to bond formation. The simulation time was set to 100 ps.

4. Hydrogens were then added back to the sites that had not formed crosslinks (step 4 in Fig. 2). Then, an energy minimisation was conducted on the system.

Although the methodology adopted is practical and fast for our purpose, it is important to highlight that these simulations cannot be related to a chemically realistic mechanism for a crosslinking process. This process has been adopted only to obtain starting geometries with varying degrees of crosslinking. This scheme allows structures to be rapidly

formed through an unphysical scheme that provides a suitable geometry matching an experimental system [60]. Moreover, such a procedure requires rapid heat removal and therefore strongly coupled thermostats are often used, such as the Berendsen thermostat [47]. Hence, while the Berendsen thermostat does not allow equilibrium properties to be accurately sampled, it is suitable for producing the starting configurations for the tensile tests.

2.1.2 Uniaxial tensile test

Reactive MD simulations were used to characterise the mechanical response of the systems. Uniaxial tensile loading was applied on selected configurations obtained during the crosslinking procedure along the x-direction at a strain rate of 10^{10} s^{-1} with a time step of 1 fs, while the y and z boundaries were controlled using the NPT equations of motion to maintain atmospheric pressure (step 5 in Fig. 2). It was verified that uniaxial tensile tests deforming in y and z directions give almost the same results due to the isotropic behaviour of the process. Periodic boundary conditions were applied to the simulation box to avoid edge effects. The environmental temperature was maintained at 300 K by using the Nosé-Hoover chains thermostat with three chains [40]. For barostating the Parrinello-Rahman barostat was used [43]. This combination accurately reproduced the dynamics of an NPT ensemble and is widely used for tensile tests with many studies published in the last year using such a procedure [12, 18, 53, 70]. Prior to loading, the system is relaxed in the NPT ensemble (300 K, 1 atm) for 100 ps to make the temperature, pressure, and other properties steady before deformation. The time step used was 1 fs and a Nosè-Hoover thermostat and a Parrinello-Rahman barostat were applied to control the system temperature and pressure during the equilibration step with a time constant of 0.1 ps. Although the starting box expanded until it reaches the atmospheric pressure at the desired temperature, the density remains almost the same at the end of the equilibration step.

The stress-strain curves were plotted and the yield stress for the different samples were determined. The yield point is defined as the stress at which a material begins to deform plastically. To identify the precise location of the yield point, a numerical unloading procedure was performed at different locations along the loading path [46]. The unloading was performed by incrementally decreasing the deformation gradient applied down to the initial undeformed configuration. The failure was assigned to the last point that exhibits reversible behavior on the stress-strain curve and hence does not lead to residual stress at zero strain [46] (step 6 in Fig. 2). In Figure 3, three loading-unloading paths for the pyrene system with $CL = 3.4$ are reported as an example.

The unloading paths from point 1 and 2 led to residual stress at zero strain, indicating that the material deformed plastically during the loading process. The unloading from point 3 goes back to the original configuration with no residual stress. Therefore, point 3 was assigned as yield point in that system.

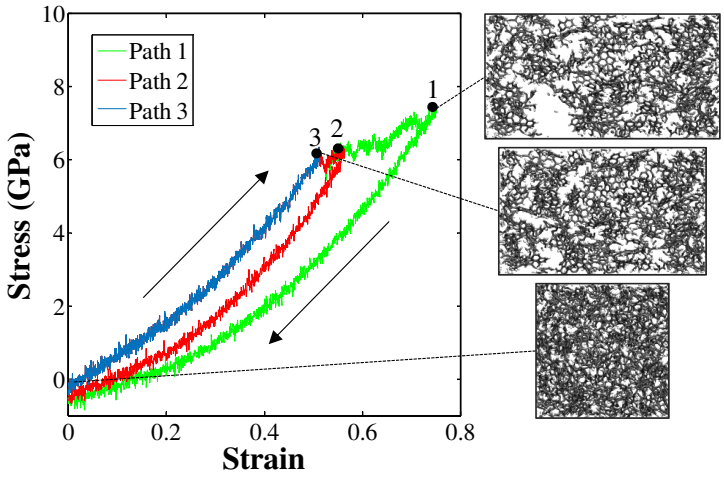

Figure 3: *Stress-strain loading and unloading curves to determine yield stress for the pyrene system with CL=3.4.*

2.1.3 Comparison with experimental values

The calculation of the hardness from the yield stress is possible by utilising an empirical conversion constant K. For many classes of materials such as metals [57] and several polymers [24] there is a linear correlation between indentation hardness (H) and yield stress (σ_f) (Eq. 2).

$$H = K\sigma_f \tag{2}$$

To convert the yield stress values in hardness, the constant K in Eq. 2 was evaluated assuming that crosslinked PAH structures have an intermediate structure between highly oriented pyrolytic graphite (HOPG) and diamond. A similar procedure to determine the yield stress was adopted on HOPG and diamond sample, and then, using the hardness values reported in Table 1, to calculate the empirical conversion constant K. Finally, the hardness values were compared with nanoindentation experiments on diesel and ethylene soot particles (Table 1) [5, 6].

2.2 High resolution transmission electron microscopy

A Yale co-flow diffusion burner was used in a standard configuration with ethylene (134.7 ml/min) and nitrogen dilution (91.2 ml/min) being supplied through the central fuel tube with an outer co-flow of air being provided through a honey comb [54]. Soot was thermophoretically sampled using an electronic solenoid to inject a holey carbon coated copper electron microscope grid into the flame. The injection was calibrated using a high speed camera to have a residence time of 30–46 ms in the flame and to not allow for condensible products to form on the grid [8].

HRTEM images were collected using a JEOL 2100F electron microscope operating at 200 kV with a resolution (point) of 0.19 nm. Only soot particles extending past the holey carbon grid into the vacuum were imaged. The magnification was constant in all pictures to allow for direct comparison of different particles fringes.

2.2.1 Fringe analysis

The HRTEM images of primary soot particles were analysed using the software previously developed and published [8]. The code was modified to allow the user to choose the centre of a primary soot particles and a radial point enclosing all fringes in a circle. This approximation excluded fringes outside the circle enclosing all fringes. Care was taken to analyse regions that were not overlapping with other soot particles order which were removed by reducing the region of interest. Five equal radii shells were then chosen from the particles centre to partition the fringes into each shell for fringe statistics to be calculated. It should be noted that the best statistics were found for the perimeter shells due partially to the increased area. We have attempted equal area shells however we decided the radial method easier to visualise with no change in the overall results. Standard error is plotted for all statistics. A total of 134 primary soot particles were analysed. This ensured the results can be considered robust which is a problem when analysing single soot particles in the flame.

2.2.2 Simulated electron microscopy images

Electron microscopy images were simulated using the multislice electron microscopy software by Kirkland [34]. Parameters used for the simulation are the following: beam energy 200 kV; objective aperture 20 mrad; (-C10)df 10 nm; ddf 20 nm; with the sampling parameters image size 1024x1024 pixels; slice thickness 0.2 nm. These parameters provide phase contrast imaging of the fringes as dark fringes.

3 Results and discussion

3.1 Hardness determined from molecular dynamics

Pyrene, coronene and ovalene structures with varying degrees of crosslinking were selected during the crosslinking procedure and MD uniaxial tensile tests were made on these selected structures. The degree of crosslinking (*CL*, Eq. 1) is reported in Fig. 4 as a function of the simulation time. Initially, there were an abundant number of reactive sites available for the crosslinking reaction, which was translated into a rapid increase of the crosslinking degree in the first picoseconds of simulation. As the reaction proceeds, less reactive sites are available for the crosslinking reaction and thus, the curve becomes almost steady reaching a value between 3.5 and 4 in all the three systems. Considering the computational costs and a limited improvement in terms of the crosslinking degree, current simulation time (100 ps) can be considered reasonable.

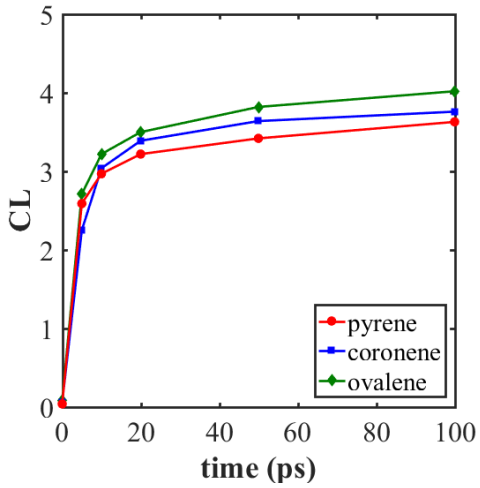

Figure 4: *Degree of crosslinking (CL) as a function of MD time for pyrene, coronene and ovalene systems.*

Figure 5 shows stress versus strain curves for these PAH structures with varying degree of crosslinking.

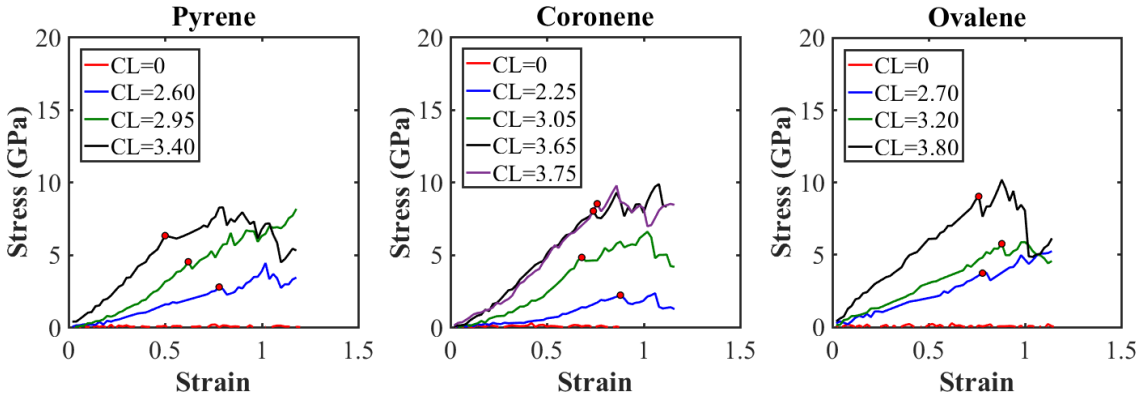

Figure 5: *Stress-strain uniaxial tensile curves for pyrene, coronene and ovalene at varying degrees of crosslinking (CL). Red circles represent the yield point in each system.*

The simulation results indicate that the tensile property increases with the degree of crosslinking. The crosslinking reaction changes some physical interactions to covalent bonds, which strengthens the mechanical properties of the sample. It is interesting to note that the tensile property of the un-crosslinked structure ($CL = 0$), *i.e.* when monomers interact only physically, is very low. A numerical unloading procedure was performed at different locations along the loading path, to identify the precise location of the yield point. The yield stresses (σ_f) obtained by the load-unload procedure for all the systems investigated are shown in Fig. 5 (red circles) and is reported in Table 2. To convert the yield stress values to hardness values, an empirical conversion constant K of 1.4 was used in Eq. 2, assuming that crosslinked PAH structures have an intermediate structure between highly oriented pyrolytic graphite (HOPG) and diamond. The yield stress for diamond

Table 2: *Yield stress and hardness values for HOPG, diamond from nanoindentation by Richter et al. [49] and the investigated crosslinked PAH structures.*

Material / PAH	*CL*	σ_f (GPa)	*H* (GPa)	*K*
HOPG	–	1.5	2.4	1.6
Diamond	–	83	100	1.2
Pyrene	0.00	0.05	0.07	1.4
	2.60	2.75	3.86	1.4
	2.95	4.20	5.88	1.4
	3.40	6.30	8.82	1.4
Coronene	0.00	0.10	0.14	1.4
	2.25	2.20	3.08	1.4
	3.05	4.90	6.72	1.4
	3.65	7.95	11.17	1.4
	3.75	8.50	11.90	1.4
Ovalene	0.00	0.10	0.14	1.4
	2.70	3.70	5.18	1.4
	3.20	5.70	7.98	1.4
	3.80	9.00	12.6	1.4

and HOPG were obtained using the same uniaxial tensile simulation conditions. Hardness values were taken from Table 1 and the corresponding *K* value were calculated using Eq. 2. The empirical conversion constant *K* was found to lie between 1.2 and 1.6. Finally, hardness was plotted as a function of the degree of crosslinking in the structure in Fig. 6. The hardness grows with the degree of crosslinking in the structure. The crosslinking

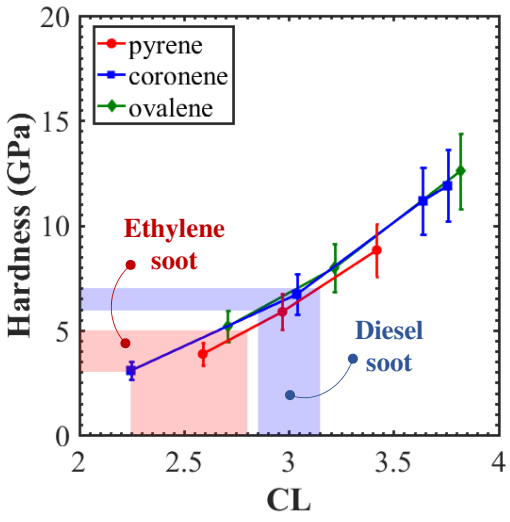

Figure 6: *Hardness versus degree of crosslinking (CL) for the emperically determined values from the reactive force field uniaxial tensile tests using K=1.4 (with error bars showing K=1.2–1.6). The hardness values determined for diesel soot and ethylene soot are also shown for comparison [5, 6].*

conversion enhances the mechanical properties of the material tested. There is a weak dependence on the extension of aromatic molecule used as monomers. For a fixed degree of crosslinking, the pyrene systems provide a lower hardness value with respect to coronene and ovalene systems indicating that the physical interactions influence, even if slightly, mechanical properties. However, moving from coronene to ovalene the curves overlap, suggesting an equal contribution of the physical interactions on the hardness value for molecules of sizes greater than or equal to coronene.

The results clearly show that the soot structure must present crosslinks between its constituent molecules to have a comparable value of the hardness found experimentally (Table 1). The results give also information on the degree of crosslinking in soot particles: $CL = 2.25 - 2.75$ for ethylene soot and $CL = 2.85 - 3.15$ for diesel soot (Fig. 6).

3.2 Internal fringe structure analysis

From the hardness of the soot and the results reported in the previous section, aliphatic crosslinks are expected between the particles. It should be noted, however, that the estimated degree of crosslinking comes from the assumption that our systems of crosslinked PAHs in a 3D network can be considered as representative of soot structure. To motivate this assumption, HRTEM images of crosslinked pyrene dimers were simulated using the multislice electron microscopy software by Kirkland [34]. The geometries and simulated fringes of crosslinked pyrene are shown in Fig. 7 at two different angles, the first at the maximum fringe contrast and the second tilted by 22.5°, and compared with the circumpyrene ones. Due to the steric hindrance of the neighbouring hydrogen to the crosslink bond, the two aromatic planes in the crosslinked pyrene cannot be parallel and, although only in a narrow range of orientations, the crosslink bond provide a kinked fringe which was lengthened with respect to the single pyrene and with a length similar to a larger PAH – circumpyrene.

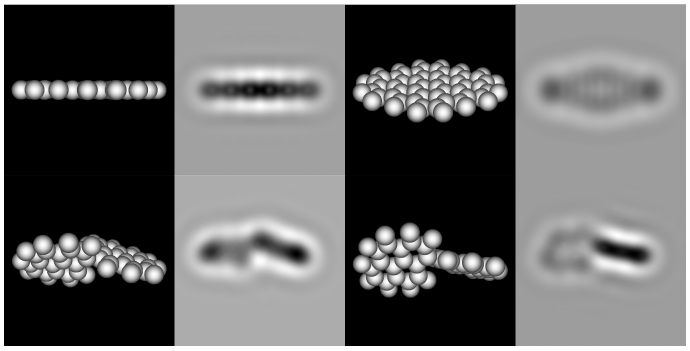

Figure 7: *Circumpyrene (top) and aliphatically-linked crosslinked pyrene (bottom) geometries with simulated transmission electron microscopy images to the right of each.*

Figure 8 shows skeletonised fringes determined from HRTEM images of a representative primary particle produced in an ethylene co-flow diffusion flame at 43 mm above the burner. Kinked fringes with angles similar to the simulated crosslinked pyrene can be

observed in the experimental image and have been circled in Fig 8 indicating aliphatic links are present. However, due to the required angle of the crosslinked species relative to the electron beam few of these kinks are observed, making the extraction of a crosslinked degree from the HRTEM difficult. Fringes with length > 1.5 nm that do not present kinks are also present in the particle structure (Fig. 8) indicating that the presence of long fringes come not only from the formation of aliphatic bonds but also from a ring condensation process.

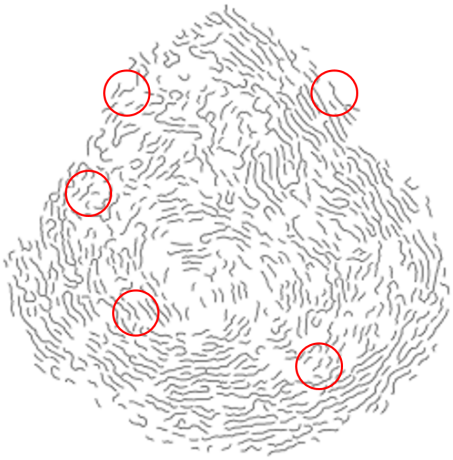

Figure 8: *Skeletonised fringes determined from HRTEM images of a soot primary particle collected at 43 mm above the burner in a ethylene co-flow diffusion flame. A selection of kinked fringes with angles similar to the crosslinked pyrene one reported in Fig. 7 have been circled in red.*

Ring condensation of PAHs are known to occur through a radical mechanism with the initial formation of an aliphatic crosslink and a following dehydrogenation reaction that leads to a new ring to be formed [36, 58, 63]:

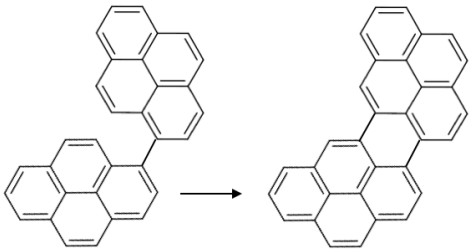

This subsequent ring formation aligns the two aromatic planes and produces a single planar PAH molecule. In carbonisation of pitch [11, 36] lengthening of the fringes is considered to be primarily due to these structures. For combustion carbons, thermal treatment of soot at 1350 °C for 10 minutes produced fringes 6 nm in length while higher temperatures $>$1950 °C gave fringe lengths $>$15 nm [64]. It is clear that the degree of carbonisation has not advanced to this degree which is expected from the short residence time in the flame (38 ms for a soot particle at the tip from our simulations of the flame

[9]) and also confirmed by fringes up to 6 nm found in the collected soot primary particles indicating a low degree of ring formation. It is interesting that the lengthening of the fringes in soot particles observed with soot maturity and increasing flame temperature is often used to indicate the crosslinking of the surface of soot primary particles. We find however that this is due to subsequent reactions and cannot be used directly to describe the degree of crosslinking which is largely unable to be viewed using HRTEM due to the unlikeliness of observing fringes with kinks. The lengenthening of fringes, however, does indicate crosslinking has preceeded the ring condensation and therefore is an indirect measure of soot crosslinking.

Figure 1, shown earlier, shows some representative skeletonised fringes from primary soot particles along the wings of a co-flow diffusion flame and as has been mentioned reveals the core-shell structure of the soot primary particles. The development of a core-shell structure has also been correlated with the maturity of the particle [33]. Therefore we analysed the radial distribution of fringe lengths and fringe spacings. While fringe lengths have been plotted as a function of radial distance previously [59] full statistics of the radial statistics for the soot particles has not yet been analysed and can provide significant insight on the core-shell structure and how it develops as soot matures. Figure 9 graphs the mean fringe length and fringe spacing for normalised radial shells for many primary soot particles at different heights above the burner (HAB). Fringe lengths were all found to be significantly longer around the perimeter 1.3–1.6 nm compared with 1.0–1.1 nm for the innermost central shell.

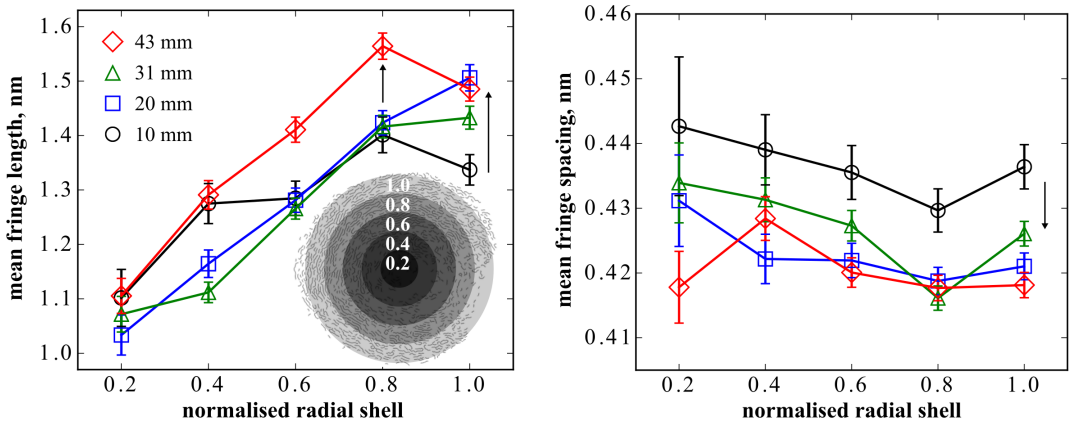

(a) Mean fringe length

(b) Mean fringe spacing

Figure 9: *Quantitative fringe analysis as a function of radial shells in primary particles in an ethylene coflow diffusion flame for the four heights shown in Figure 1. Inset shows the normalised radial shells within which the fringe statistics are computed.*

A general trend was seen towards increasing fringe length as the soot matured (for the 1.0 radial shell increasing by 0.2 nm) this would indicate carbonisation occurring as the soot was held at elevated temperatures. The structural difference between the internal and external fringes, however, was also present for the lowest height, where the smallest primary particles (∼10 nm) are found. This suggests that the transition from nuclei particles

(<3 nm) to primary particles (∼10 nm) proceeds through a rapid carbonisation occurring from the outside in, early in the flame. The fringe interspacing distance (often quoted as d_{002} if compared with x-ray diffraction) decreased as a function of HAB (Fig. 9(b)). For the lowest HAB the fringe spacings spanned 0.43–0.45 nm with a decrease found for the 20 mm HAB and above leading to a reduction in the distances 0.42–0.43 nm. These values also indicate that a crosslinking and carbonisation process is occurring.

The presence of a kinked fringe as well as the lengthening of the fringe leads to the conclusion that the soot formation mechanism involves a crosslinking process followed by a carbonisation process. We can also state that the soot particle's structure is a 3D network of crosslinked PAHs, especially in the early stages of soot formation where crosslinking is predominant. Although the structures simulated in the previous section are not fully representative of soot as they are composed of homogeneous molecules that would lead to observed fringes with same length, the lack of sensitivity between the PAH size on the hardness-crosslink relationship suggests that the results from the previous section would not be significantly affected by a heterogeneous system. We have also not explored how curved aromatics, known to be present in soot, integrate into a crosslinked structure. This could have implications for the nanoscale properties of these materials introducing, for example, flexoelectricity [38]. However, we aim to extend this analysis in subsequent work.

4 Conclusions

The degree of crosslinking in combustion carbons was explored using reactive MD uniaxial tensile simulations of pyrene, coronene and ovalene at varying degrees crosslinking with a weak dependence on the size of the fragment found. An empirical relationship between the nanoindentation hardness and uniaxial tensile failure stress was determined from diamond and HOPG references and found to lie between $K = 1.2 - 1.6$. Ethylene soot are then expected to have crosslinked densities between $2.25 - 2.75$ and diesel soot considered to have a crosslinked density between $2.85 - 3.15$ to have a comparable value of the hardness found from nanoindentation experiments. These results suggest that nanoindentation experiments on nascent soot particles could provide insight into whether they are liquid like (un-crosslinked) or carbonised (crosslinked).

HRTEM images of primary soot particles and simulated images of crosslinked PAHs provide evidence for aliphatic linkages from the presence of kinked fringes in HRTEM images of primary soot particles. Further elongation of the fringes indicates a carbonisation process which we studied by probing the electron micrograph fringe statistics as a function of radial distance for the first time. Fringe length was found to increase and interfringe distance decrease with the radial distance for all the HAB, giving evidence for the core-shell structure early in the flame. Further evidence for carbonisation is found as fringes increase in length for increased HAB.

In conclusion, the hardness of soot, the presence of kinked fringes in HRTEM images and the lengthening of fringes suggest that the soot formation mechanism involves a crosslinking process followed by a carbonisation process – important processes that take place in combustion – and that a 3D network of crosslinked PAHs is present in soot structure.

Acknowledgements

This project is supported by the National Research Foundation (NRF), Prime Minister's Office, Singapore under its Campus for Research Excellence and Technological Enterprise (CREATE) programme.

References

[1] M. Alfè, B. Apicella, A. Tregrossi, and A. Ciajolo. Identification of large polycyclic aromatic hydrocarbons in carbon particulates formed in a fuel-rich premixed ethylene flame. *Carbon*, 46(15):2059–2066, 2008. doi:10.1016/j.carbon.2008.08.019.

[2] M. Alfè, B. Apicella, R. Barbella, J. Rouzaud, A. Tregrossi, and A. Ciajolo. Structure–property relationship in nanostructures of young and mature soot in premixed flames. *Proceedings of the Combustion Institute*, 32:697–704, 2009. doi:10.1016/j.proci.2008.06.193.

[3] M. Alfè, B. Apicella, J. Rouzaud, A. Tregrossi, and A. Ciajolo. The effect of temperature on soot properties in premixed methane flames. *Combustion and Flame*, 157:1959–1965, 2010. doi:10.1016/j.combustflame.2010.02.007.

[4] B. Apicella, P. Pré, M. Alfè, A. Ciajolo, V. Gargiulo, C. Russo, A. Tregrossi, D. Deldique, and J. Rouzaud. Soot nanostructure evolution in premixed flames by High Resolution Electron Transmission Microscopy (HRTEM). *Proceedings of the Combustion Institute*, 35(2):1895–1902, 2015. doi:10.1016/j.proci.2014.06.121.

[5] H. Bhowmick and S. K. Biswas. Relationship between physical structure and tribology of single soot particles generated by burning ethylene. *Tribology Letters*, 44(2): 139–149, 2011. doi:10.1007/s11249-011-9831-5.

[6] H. Bhowmick, S. K. Majumdar, and S. K. Biswas. Dry tribology and nanomechanics of gaseous flame soot in comparison with carbon black and diesel soot. *Proceedings of the Institution of Mechanical Engineers, Part C: Journal of Mechanical Engineering Science*, 226(2):394–402, 2011. doi:10.1177/0954406211429410.

[7] T. C. Bond, S. J. Doherty, D. W. Fahey, P. M. Forster, T. Berntsen, B. J. Deangelo, M. G. Flanner, S. Ghan, B. Kärcher, D. Koch, S. Kinne, Y. Kondo, P. K. Quinn, M. C. Sarofim, M. G. Schultz, M. Schulz, C. Venkataraman, H. Zhang, S. Zhang, N. Bellouin, S. K. Guttikunda, P. K. Hopke, M. Z. Jacobson, J. W. Kaiser, Z. Klimont, U. Lohmann, J. P. Schwarz, D. Shindell, T. Storelvmo, S. G. Warren, and C. S. Zender. Bounding the role of black carbon in the climate system: A scientific assessment. *Journal of Geophysical Research Atmospheres*, 118(11):5380–5552, 2013. doi:10.1002/jgrd.50171.

[8] M. L. Botero, D. Chen, S. González-Calera, D. Jefferson, and M. Kraft. HRTEM evaluation of soot particles produced by the non-premixed combustion of liquid fuels. *Carbon*, 96:459–473, 2016. doi:10.1016/j.carbon.2015.09.077.

[9] M. L. Botero, N. Eaves, J. A. Dreyer, Y. Sheng, J. Akroyd, W. Yang, and M. Kraft. Experimental and numerical study of the evolution of soot primary particles in a diffusion flame. *Proceedings of the Combustion Institute*, 41(in press), 2018. doi:10.1016/S0032-3861(99)00755-7.

[10] D. W. Brenner, O. A. Shenderova, J. A. Harrison, S. J. Stuart, B. Ni, and S. B. Sinnott. A second–generation reactive empirical bond order (REBO) potential energy expression for hydrocarbons. *Journal of Physics: Condensed Matter*, 14(4): 783–802, 2002. doi:10.1088/0953-8984/14/4/312.

[11] P. R. Buseck, B. Huang, and L. P. Keller. Electron microscope investigation of the structures of annealed carbons. *Energy & Fuels*, 1(1):105–110, 1987. doi:10.1021/ef00001a020.

[12] L. Chang, C.-Y. Zhou, L.-L. Wen, J. Li, and X. H. He. Molecular dynamics study of strain rate effects on tensile behavior of single crystal titanium nanowire. *Computational Materials Science*, 128:348–358, 2017. doi:10.1016/j.commatsci.2016.11.034.

[13] S.-H. Chung and A. Violi. Peri–condensed aromatics with aliphatic chains as key intermediates for the nucleation of aromatic hydrocarbons. *Proceedings of the Combustion Institute*, 33(1):693–700, 2011. doi:10.1016/j.proci.2010.06.038.

[14] A. Ciajolo, B. Apicella, R. Barbella, and A. Tregrossi. Correlations of the spectroscopic properties with the chemical composition of flame–formed aromatic mixtures. *Combustion Science and Technology*, 153:19–32, 2000. doi:10.1080/00102200008947248.

[15] M. Commodo, G. De Falco, A. Bruno, C. Borriello, P. Minutolo, and A. D'Anna. Physicochemical evolution of nascent soot particles in a laminar premixed flame: from nucleation to early growth. *Combustion and Flame*, 162(10):3854–3863, 2015.

[16] A. D'Anna. Combustion-formed nanoparticles. *Proceedings of the Combustion Institute*, 32(1):593 – 613, 2009. doi:https://doi.org/10.1016/j.proci.2008.09.005.

[17] R. Dastanpour, A. Momenimovahed, K. Thomson, J. Olfert, and S. Rogak. Variation of the optical properties of soot as a function of particle mass. *Carbon*, 124:201–211, 2017. doi:10.1016/j.carbon.2017.07.005.

[18] C. de Tomas, I. Suarez-Martinez, and N. A. Marks. Carbide-derived carbons for dense and tunable 3D graphene networks. *Applied Physics Letters*, 112(25):251907, 2018. doi:10.1063/1.5030136.

[19] R. A. Dobbins, R. A. Fletcher, and H.-C. Chang. The evolution of soot precursor particles in a diffusion flame. *Combustion and Flame*, 115(3):285–298, 1998. doi:10.1016/S0010-2180(98)00010-8.

[20] J. Donnet, J. Schultz, and A. Eckhardt. Etude de la microstructure d'un noir de carbone thermique. *Carbon*, 6(6):781–788, 1968. doi:10.1016/0008-6223(68)90064-X.

[21] P. Elvati and A. Violi. Thermodynamics of poly-aromatic hydrocarbon clustering and the effects of substituted aliphatic chains. *Proceedings of the Combustion Institute*, 34(1):1837–1843, 2013. doi:10.1016/j.proci.2012.07.030.

[22] P. Elvati and A. Violi. Homo–dimerization of oxygenated polycyclic aromatic hydrocarbons under flame conditions. *Fuel*, 222:307–311, 2018. doi:10.1016/j.fuel.2018.02.095.

[23] X. Fan, K. Nose, D. Diao, and T. Yoshida. Nanoindentation behaviors of amorphous carbon films containing nanocrystalline graphite and diamond clusters prepared by radio frequency sputtering. *Applied Surface Science*, 273:816–823, 2013. doi:10.1016/j.apsusc.2013.03.012.

[24] A. Flores, F. J. B. Calleja, G. E. Attenburrow, and D. C. Bassett. Microhardness studies of chain-extended pe: Iii. correlation with yield stress and elastic modulus. *Polymer*, 41(14):5431–5435, 2000. doi:10.1016/S0032-3861(99)00755-7.

[25] M. Frenklach. Reaction mechanism of soot formation in flames. *Physical Chemistry Chemical Physics*, 4(11):2028–2037, 2002. doi:10.1039/B110045A.

[26] M. Frenklach and H. Wang. Detailed modeling of soot particle nucleation and growth. *Symposium (International) on Combustion*, 23(1):1559–1566, 1991. doi:10.1016/S0082-0784(06)80426-1.

[27] F. A. Heckman and D. F. Harling. Progressive oxidation of selected particles of carbon black: further evidence for a new microstructural model. *Rubber Chemistry and Technology*, 39(1):1–13, 1966. doi:10.5254/1.3544829.

[28] R. D. Heidenreich, W. M. Hess, and L. L. Ban. A test object and criteria for high resolution electron microscopy. *Journal of Applied Crystallography*, 1(1):1–19, 1968. doi:10.1107/S0021889868004930.

[29] J. D. Herdman and J. H. Miller. Intermolecular potential calculations for polynuclear aromatic hydrocarbon clusters. *The Journal of Physical Chemistry A*, 112(28):6249–6256, 2008. doi:10.1021/jp800483h.

[30] K.-H. Homann. Fullerenes and soot formation – new pathways to large particles in flames. *Angewandte Chemie International Edition*, 37(18): 2434–2451, 1998. doi:10.1002/(SICI)1521-3773(19981002)37:18<2434::AID-ANIE2434>3.0.CO;2-L.

[31] T. Ishiguro, Y. Takatori, and K. Akihama. Microstructure of diesel soot particles probed by electron microscopy: First observation of inner core and outer shell. *Combustion and Flame*, 108(1-2):231–234, 1997. doi:10.1016/S0010-2180(96)00206-4.

[32] N. Iwashita and M. V. Swain. Elasto-plastic deformation of glassy carbon by nanoindentation with spherical tipped indenters. *Molecular Crystals and Liquid Crystals*, 386:39–44, 2002. doi:10.1080/10587250290113169.

[33] M. R. Kholghy, A. Veshkini, and M. J. Thomson. The core-shell internal nanostructure of soot - A criterion to model soot maturity. *Carbon*, 100:508–536, 2016. doi:10.1016/j.carbon.2016.01.022.

[34] E. J. Kirkland. *Advanced computing in electron microscopy*. Springer Science & Business Media, 2010.

[35] P. J. Landrigan, R. Fuller, N. J. R. Acosta, O. Adeyi, R. Arnold, N. N. Basu, A. B. Baldé, R. Bertollini, S. Bose-O'Reilly, J. I. Boufford, P. N. Breysse, T. Chiles, C. Mahidol, A. M. Coll-Seck, M. L. Cropper, J. Fobil, V. Fuster, M. Greenstone, A. Haines, D. Hanrahan, D. Hunter, M. Khare, A. Krupnick, B. Lanphear, B. Lohani, K. Martin, K. V. Mathiasen, M. A. McTeer, C. J. L. Murray, J. D. Ndahimananjara, F. Perera, J. Potočnik, A. S. Preker, J. Ramesh, J. Rockström, C. Salinas, L. D. Samson, K. Sandilya, P. D. Sly, K. R. Smith, A. Steiner, R. B. Stewart, W. A. Suk, O. C. P. van Schayck, G. N. Yadama, K. Yumkella, and M. Zhong. The Lancet Commission on pollution and health. *The Lancet*, 2017. doi:10.1016/S0140-6736(17)32345-0.

[36] I. C. Lewis. Thermal polymerization of aromatic hydrocarbons. *Carbon*, 18(3): 191–196, 1980. doi:10.1016/0008-6223(80)90060-3.

[37] Q. Mao, A. C. T. van Duin, and K. H. Luo. Formation of incipient soot particles from polycyclic aromatic hydrocarbons: A ReaxFF molecular dynamics study. *Carbon*, 121:380–388, 2017. doi:10.1016/j.carbon.2017.06.009.

[38] J. W. Martin, R. I. Slavchov, E. K. Y. Yapp, J. Akroyd, S. Mosbach, and M. Kraft. The Polarization of Polycyclic Aromatic Hydrocarbons Curved by Pentagon Incorporation: The Role of the Flexoelectric Dipole. *The Journal of Physical Chemistry C*, 121(48):27154–27163, 2017. doi:10.1021/acs.jpcc.7b09044.

[39] L. Martinez, R. Andrade, E. G. Birgin, and J. M. Martínez. PACKMOL: A package for building initial configurations for molecular dynamics simulations. *Journal of Computational Chemistry*, 30(13):2157–2164, 2009. doi:10.1002/jcc.21224.

[40] G. J. Martyna, M. L. Klein, and M. Tuckerman. Nosè–Hoover chains: The canonical ensemble via continuous dynamics. *The Journal of Chemical Physics*, 97(4):2635–2643, 1992. doi:10.1063/1.463940.

[41] J. R. McConnell, R. Edwards, G. L. Kok, M. G. Flanner, C. S. Zender, E. S. Saltzman, J. R. Banta, D. R. Pasteris, M. M. Carter, and J. D. W. Kahl. 20th-century industrial black carbon emissions altered arctic climate forcing. *Science*, 317(5843): 1381–1384, 2007. doi:10.1126/science.1144856.

[42] T. C. O'Connor, J. Andzelm, and M. O. Robbins. AIREBO-M: A reactive model for hydrocarbons at extreme pressures. *The Journal of Chemical Physics*, 142(2): 024903, 2015. doi:10.1063/1.4905549.

[43] M. Parrinello and A. Rahman. Polymorphic transitions in single crystals: A new molecular dynamics method. *Journal of Applied Physics*, 52:7182–7190, 1981. doi:10.1063/1.328693.

[44] J. R. Patterson, S. A. Catledge, Y. K. Vohra, J. Akella, and S. T. Weir. Electrical and mechanical properties of C_{70} fullerene and graphite under high pressures studied using designer diamond anvils. *Physical Review Letters*, 85(25):5364–5367, 2000. doi:10.1103/PhysRevLett.85.5364.

[45] S. Plimpton. Fast parallel algorithms for short-range molecular dynamics. *Journal of Computational Physics*, 117(1):1–19, 1995. doi:10.1006/jcph.1995.1039.

[46] M. J. A. Qomi, D. Ebrahimi, M. Bauchy, R. Pellenq, and F.-J. Ulm. Methodology for estimation of nanoscale hardness via atomistic simulations. *Journal of Nanomechanics and Micromechanics*, 7(4):04017011, 2017. doi:10.1061/(ASCE)NM.2153-5477.0000127.

[47] R. Ranganathan, S. Rokkam, T. Desai, and P. Keblinski. Generation of amorphous carbon models using liquid quench method: A reactive molecular dynamics study. *Carbon*, 113:87–99, 2017. doi:10.1016/j.carbon.2016.11.024.

[48] M. Rapacioli, F. Calvo, F. Spiegelman, C. Joblin, and D. J. Wales. Stacked clusters of polycyclic aromatic hydrocarbon molecules. *The Journal of Physical Chemistry A*, 109(11):2487–2497, 2005. doi:10.1021/jp046745z.

[49] A. Richter, R. Riesa, R. Smith, M. Henkel, and B. Wolf. Nanoindentation of diamond, graphite and fullerene films. *Diamond and Related Materials*, 9:170–184, 2000. doi:10.1016/S0925-9635(00)00188-6.

[50] H. Richter, T. G. Benish, O. A. Mazyar, W. H. Green, and J. B. Howard. Formation of polycyclic aromatic hydrocarbons and their radicals in a nearly sooting premixed benzene flame. *Proceedings of the Combustion Institute*, 28(2):2609–2618, 2000. doi:10.1016/S0082-0784(00)80679-7.

[51] C. Schuetz and M. Frenklach. Nucleation of soot: molecular dynamics simulations of pyrene dimerization. *Proceedings of the Combustion Institute*, 29:2307–2313, 2002. doi:10.1016/S1540-7489(02)80281-4.

[52] A. D. Sediako, C. Soong, J. Y. Howe, M. R. Kholghy, and M. J. Thomson. Real-time observation of soot aggregate oxidation in an Environmental Transmission Electron Microscope. *Proceedings of the Combustion Institute*, 36(1):841–851, 2017. doi:10.1016/j.proci.2016.07.048.

[53] E. Shahini, K. K. Taheri, and A. K. Taheri. An investigation on tensile properties of coiled carbon nanotubes using molecular dynamics simulation. *Diamond and Related Materials*, 74:154–163, 2017. doi:10.1016/j.diamond.2017.02.023.

[54] M. D. Smooke, C. S. McEnally, L. D. Pfefferle, R. J. Hall, and M. B. Colket. Computational and experimental study of soot formation in a coflow, laminar diffusion flame. *Combustion and Flame*, 117(1):117–139, 1999. doi:10.1016/S0010-2180(98)00096-0.

[55] S. J. Stuart, A. B. Tutein, and J. A. Harrison. A reactive potential for hydrocarbons with intermolecular interactions. *The Journal of Chemical Physics*, 112(14):6472–6486, 2000. doi:10.1063/1.481208.

[56] C. W. Sweitzer and G. L. Heller. The formation of carbon black in hydrocarbon flames. *Rubber World*, 134:855–865, 1956.

[57] D. Tabor. *The hardness of metals*. Clarendon Press, 1951.

[58] A. V. Talyzin, S. M. Luzan, K. Leifer, S. Akhtar, J. Fetzer, F. Cataldo, Y. O. Tsybin, C. W. Tai, A. Dzwilewski, and E. Moons. Coronene fusion by heat treatment: Road to nanographenes. *The Journal of Physical Chemistry C*, 115(27):13207–13214, 2011. doi:10.1021/jp2028627.

[59] P. D. Teini, D. M. Karwat, and A. Atreya. Observations of nascent soot: Molecular deposition and particle morphology. *Combustion and Flame*, 158(10):2045–2055, 2011. doi:10.1016/j.combustflame.2011.03.005.

[60] M. W. Thompson, B. Dyatkin, W. H. W, C. H. Turner, X. Sang, R. R. Unocic, C. R. Iacovella, Y. Gogotsi, A. C. T. van Duin, and P. T. Cummings. An atomistic carbide-derived carbon model generated using ReaxFF-based quenched Molecular Dynamics. *C*, 4(3):32, 2017. doi:10.3390/c3040032.

[61] T. S. Totton, D. Chakrabarti, A. J. Misquitta, M. Sander, D. J. Wales, and M. Kraft. Modelling the internal structure of nascent soot particles. *Combustion and Flame*, 157(5):909–914, 2010. doi:10.1016/j.combustflame.2009.11.013.

[62] T. S. Totton, A. J. Misquitta, and M. Kraft. A quantitative study of the clustering of polycyclic aromatic hydrocarbons at high temperatures. *Physical chemistry chemical physics*, 14(12):4081–4094, 2012. doi:10.1039/c2cp23008a.

[63] B. V. Unterreiner, M. Sierka, and R. Ahlrichs. Reaction pathways for growth of polycyclic aromatic hydrocarbons under combustion conditions, a DFT study. *Physical Chemistry Chemical Physics*, 6(18):4377–4384, 2004. doi:10.1039/b407279k.

[64] R. L. Vander Wal, A. J. Tomasek, K. Street, D. R. Hull, and W. K. Thompson. Carbon Nanostructure Examined by Lattice Fringe Analysis of High-Resolution Transmission Electron Microscopy Images. *Applied Spectroscopy*, 58(2):230–237, 2004. doi:10.1366/000370204322842986.

[65] A. Violi, A. Kubota, T. Truong, W. Pitz, C. Westbrook, and A. Sarofim. A fully integrated kinetic monte carlo/molecular dynamics approach for the simulation of soot precursor growth. *Proceedings of the Combustion Institute*, 29(2):2343–2349, 2002. doi:10.1016/S1540-7489(02)80285-1.

[66] A. Violi, A. F. Sarofim, and G. A. Voth. Kinetic Monte Carlo-molecular dynamics approach to model soot inception. *Combustion Science and Technology*, 176(5-6): 991–1005, 2004. doi:10.1080/00102200490428594.

[67] H. Wang. Formation of nascent soot and other condensed-phase materials in flames. *Proceedings of the Combustion Institute*, 33(1):41–67, 2011. doi:10.1016/j.proci.2010.09.009.

[68] R. Whitesides and M. Frenklach. Detailed kinetic Monte Carlo simulations of graphene-edge growth. *The Journal of Physical Chemistry. A*, 114(2):689–703, 2010. doi:10.1021/jp906541a.

[69] E. K. Yapp, C. G. Wells, J. Akroyd, S. Mosbach, R. Xu, and M. Kraft. Modelling PAH curvature in laminar premixed flames using a detailed population balance model. *Combustion and Flame*, 176:172–180, 2017. doi:10.1016/j.combustflame.2016.10.004.

[70] F. Zhang and J. Zhou. Molecular dynamics study of bimodal nanotwinned cu with a composite structure. *Computational Materials Science*, 145:60–67, 2018. doi:10.1016/j.commatsci.2017.12.060.

[71] H. B. Zhang, X. You, H. Wang, and C. K. Law. Dimerization of polycyclic aromatic hydrocarbons in soot nucleation. *The Journal of Physical Chemistry A*, 118(8): 1287–1292, 2014. doi:10.1021/jp411806q.

[72] B. Zhao, K. Uchikawa, and H. Wang. A comparative study of nanoparticles in premixed flames by scanning mobility particle sizer, small angle neutron scattering, and transmission electron microscopy. *Proceedings of the Combustion Institute*, 31: 851–860, 2007. doi:10.1016/j.proci.2006.08.064.

[73] G. A. Zickler, T. Schöberl, and O. Paris. Mechanical properties of pyrolysed wood: a nanoindentation study. *Philosophical Magazine*, 86(10):1373–1386, 2006. doi:10.1080/14786430500431390.